Available online at www.sciencedirect.com

ScienceDirect

Advances in Space Research xxx (xxxx) xxx

ADVANCES IN SPACE RESEARCH (a COSPAR publication)

www.elsevier.com/locate/asr

A satellite-centered criticality index for post-fragmentation environmental hazard assessment using toroidal regions

L. De Maria [a,*], A. De Vittori [b], P. Di Lizia [a], M. Massari [a]

[a] Department of Aerospace Science and Technology, Politecnico di Milano, Via G. La Masa 34, Milan 20156, Italy
[b] School of Aeronautics and Astronautics, Purdue University, 701 W, Stadium Ave, West Lafayette 47907, IN, USA

Received 16 February 2026; received in revised form 25 May 2026; accepted 16 June 2026

Abstract

Ensuring the operational safety of a space asset requires continuous conjunction assessment and, when necessary, the execution of Collision Avoidance Manoeuvrers based on catalogued tracking data. Fragmentation events, such as explosions or collisions, pose a distinct challenge, as they can suddenly generate thousands of debris dispersed across a broad range of orbital altitudes. If an asset intersects such a cloud, the collision probability may increase dramatically, potentially leading to mission failure and further fragmentations. Risk assessment in the immediate aftermath is particularly challenging due to the high number of untracked fragments and the time required to estimate their trajectories. To address this limitation, the present study introduces the Criticality of Neighbourhood Index (CNI), a novel environmental hazard metric focused on a single asset in Low Earth Orbit. Building upon the Criticality of Spacecraft Index and Shell Criticality, the CNI quantifies the risk associated with remaining on the nominal orbit following a nearby fragmentation and identifies potentially safer orbital altitudes. The starting point is the definition of a toroidal region centred on the asset's orbit, from which successive contiguous and concentric toroids are introduced at higher and lower orbits. Hereafter, the index is quantified by simulating the fragmentation with the NASA Standard Break-up Model, propagating the resulting debris distribution and computing their effects on each toroid. The proposed approach enables short-term hazard prediction in the vicinity of an asset while requiring limited computational resources and only high-level information about the fragmentation event.

Keywords: Space situational awareness; Fragmentation; Environmental criticality; Space debris environment

1. Introduction

Quantifying the level of risk posed by space debris across different orbital regimes, and to the active satellites operating within them, has been the focus of numerous studies in recent years. The development of a standardized index to assess the environmental safety of orbital regions, as well as the impact of debris-generating events, would significantly strengthen Space Surveillance and Tracking (SST) capabilities. Such an index would enable more effective monitoring of current orbital conditions and support reliable short- to medium-term forecasts of their evolution.

The primary difficulty lies in defining an appropriate set of parameters, and their associated computational methodologies, that can accurately capture the environmental impact of individual objects. A further complication is ensuring that the approach remains highly computationally efficient, given the vast number of objects currently present in orbit and the long propagation times possibly involved.

* Corresponding author.
E-mail addresses: luigi.demaria@polimi.it (L. De Maria), adevitto@purdue.edu (A. De Vittori), pierluigi.dilizia@polimi.it (P. Di Lizia), mauro.massari@polimi.it (M. Massari).

https://doi.org/10.1016/j.asr.2026.06.050
0273-1177/

In Utzmann et al. (2012), authors introduce an index called Figure of Merit (FoM) which is the product of the collision flux in the object's orbit, the target mass and cross-section, and the orbital lifetime. Building upon this work, Pardini and Anselmo (2016) propose a similar formulation focused on rocket bodies abandoned in Low Earth Orbit (LEO) with the purpose of identifying the most suitable candidates for future Active Debris Removal (ADR) missions. In a successive work, Anselmo and Pardini (2017) introduce a normalized ranking index, to prioritize the ADR target selection, composed of two functions taking into account the probability of collision-induced break-up and the long-term impact of produced fragments on the environment. Similarly, Kebschull et al. (2017) proposes an index obtained by multiplying the probability of collision and an environmental damage factor considering the variation in environmental flux due to the introduction of the collision fragments.

Another widely explored index is the Environmental Consequences of Orbital Break-ups (ECOB) presented in Letizia et al. (2016), which quantifies the effect of spacecraft's catastrophic break-up on the debris environment. ECOB is computed by simulating a break-up cloud and summing the collision probabilities of the fragments on a representative set of active satellites. The index is extended in Letizia et al. (2017) by considering not only the effect of the fragmentation but also its likelihood. It is also employed for space missions Life Cycle Assessment in Colombo et al. (2017) and severity metric in Muciaccia et al. (2025), where also constellations are included. Servadio et al. (2024) introduces the MIT Risk Index (MITRI), considering each object's altitude, orbital lifetime, collision probability, and estimated number and mass of debris it would produce during a fragmentation. Results show that MITRI agrees with other indexes, however it differently characterizes the debris with highest threat.

In Rossi et al. (2015), authors present the Criticality of Spacecraft Index (CSI) to rank the long-term environmental criticality of abandoned LEO objects. It is an analytical metric based on dividing the region of interest into shells and computing the criticality by combining objects' masses, inclinations, orbital lifetimes and local environmental debris densities. Such index is expanded in Bombardelli et al. (2017) as Shell Criticality, to account for objects' eccentricities by introducing a fractional term of orbital period spent into a shell. The new CSI is successively applied to a debris repositioning scenario. Also constellations and their environmental impact are investigated with such a metric in Rossi et al. (2020), with the definition of the Criticality of Constellation Index (CCI) in Rossi et al. (2017) as a special case of CSI. Finally, in Rossi et al. (2022), through the object's cross-sectional area, the trackability of objects is accounted for in the definition of CSI, which embeds the current SST limitations.

The objective of this research is to develop a procedure capable of rapidly assessing the risk of collisions of a specific satellite with fragments immediately following a generating event. This is achieved by employing a modified version of the CSI (Rossi et al., 2015) and the Shell Criticality (Bombardelli et al., 2017; Rossi et al., 2022) to define an index able to provide a practical quantification mean of the short-term effects of break-up events, and in general space debris, on specific satellites, while requiring only limited computational resources. Named Criticality of Neighbourhood Index (CNI), it evaluates the safety level of the surrounding orbital space of an asset using co-planar toroidal regions, it determines the necessity of an orbital manoeuvrer, and, if required, identifies the nearest altitude that satisfies a prescribed safety threshold.

The fundamental concepts underpinning the present analysis are introduced in Section 2, followed by the definition of the CNI in Section 3. The simulation framework and corresponding results are presented and discussed for two test cases: the COSMOS 1408 break-up in Section 4 and the IRIDIUM 33-COSMOS 2251 collision in Section 5. Concluding remarks, together with perspectives for future developments are provided in Section 6.

2. Fundamentals

In this section, the mathematical background of reference frames and dynamics employed in this work are presented.

2.1. Reference frames

The first and fundamental reference frame employed in this work is the Earth-Centered Inertial (ECI), also referred to as geocentric equatorial coordinate system. It is defined by placing the origin in the Earth's centre of mass and defining the x-axis as the vernal equinox direction, the z-axis in the direction of the north-pole, and y-axis completes the orthogonal triad.

Successively, in order to determine whether a fragment enters the satellite's toroidal region, the Radial-Tangential-Normal (RTN) local coordinate system will be employed later in this study. Such a frame has the first axis $\hat{\mathbf{R}}$ aligned with the radial direction, from Earth's centre towards the satellite as it moves through its orbit; the $\hat{\mathbf{N}}$ axis normal to the orbital plane; and the $\hat{\mathbf{T}}$ completing the right-handed triad (Vallado, 2022). Their computation can be carried out as follows:

$$\hat{\mathbf{R}} = \frac{\mathbf{r}}{||\mathbf{r}||}; \quad \hat{\mathbf{N}} = \frac{\mathbf{r}\times\mathbf{v}}{||\mathbf{r}\times\mathbf{v}||}; \quad \hat{\mathbf{T}} = \hat{\mathbf{N}}\times\hat{\mathbf{R}} \tag{1}$$

$$\mathbf{r}_{RTN} = \left[\hat{\mathbf{R}}, \hat{\mathbf{T}}, \hat{\mathbf{N}}\right]\mathbf{r}_{ECI} \tag{2}$$

where $\mathbf{r}, \mathbf{v} \in \mathbb{R}^3$ are the position and velocity vectors of the generic orbiting object, respectively, and $\hat{\mathbf{R}}, \hat{\mathbf{T}}, \hat{\mathbf{N}} \in \mathbb{R}^3$ are the unit vectors defining the radial, tangential and normal directions of the RTN frame.

2.2. Dynamical models

Fragments propagation is performed using both unperturbed two-body dynamics and a higher-fidelity dynamical model. While the latter provides a more accurate description of objects' motion around the Earth, it entails a significantly higher computational cost. Consequently, the two models are employed at different stages of the analysis.

In the first phase, the high-fidelity model proposed in Morselli et al. (2014) is used to propagate the generated fragments over a 7-day interval in order to capture their realistic spatial dispersion, identify and discard fragments that reenter the Earth's atmosphere due to aerodynamic drag, and store the resulting final states. To this end, although the selected model supports a wide range of perturbative effects, only those relevant over the limited propagation window are considered. Specifically, the Earth's gravitational field is modelled using spherical harmonics up to the J_2 term, and atmospheric drag is included assuming air density computed through Naval Research Laboratory's Mass Spectrometer and Incoherent Scatter Radar of year 2000 (NRLMSISE-00) model (Picone et al., 2002) and rotating atmosphere.

In the subsequent phase, as detailed in Section 3.3, the Residence Time term is evaluated through the unperturbed two-body dynamics, using as initial states those stored previously. Since the propagation interval associated with this term corresponds to each fragment's orbital period, the relatively short time horizon limits the error introduced by the simplified dynamical model. This choice ensures the computational efficiency of the CNI routine, which is meant for rapidly processing a large number of objects possibly for multiple satellites at a time.

3. The criticality of neighbourhood index

As stated in Section 1, the CNI represents a specialization of the CSI, introduced in Bombardelli et al. (2017), designed to assess the safety level in the immediate vicinity of a satellite. Previous studies (Rossi et al., 2022) focused on dividing the LEO region into spherical shells and computing the Shell Criticality by cumulatively summing the CSI of all objects transiting each shell. This approach enables a global assessment of the environmental hazard posed by objects adrift, incorporating both their orbital and physical characteristics.

However, due to its inherently global nature, the Shell Criticality framework is not well-suited for determining whether a specific satellite should execute an orbital manoeuvrer in response to a debris-generating event. To address this limitation, the CNI selects and modifies a subset of the terms in the original CSI formulation, focusing only on those relevant for short-term, localized risk assessments.

The method proceeds by defining a series of $N \in \mathbb{N}^+$ concentric and contiguous toroidal regions (with quasi-rectangular cross-sections) centred on the orbit of the satellite under consideration. Each toroid, stated in the formulation with the subscript $j \in \mathbb{N}^+$, is characterized by a specific width and height, corresponding to the chosen altitude interval, $\Delta h \in \mathbb{R}^+$, and thickness of orbital inclination surrounding the satellite's nominal orbit, $\Delta i \in \mathbb{R}$, respectively. Although various selections for these parameters are possible, a robust approach entails setting the width and height equal to the radii of the radial cross-section of the asset's position covariance ellipsoid. Consequently, this configuration inherently embeds the satellite's positional uncertainty within the toroid's dimensions.

An explanatory scheme is depicted in Fig. 1, where a single toroid is depicted. The final method will consider several of these toroids, forming a disk centred in the Earth and covering a user-define range of altitudes.

3.1. Physical properties terms

The first term considered is the most influential physical parameter: the object's mass, $m \in \mathbb{R}^+$. The formulation is kept identical to the classical CSI presented in Rossi et al. (2015), for which:

$$M_k = \frac{m_k}{m_0} \tag{3}$$

where m_k is the mass of the k-th fragment, with $k \in \mathbb{N}^+$, and $m_0 \in \mathbb{R}^+$ is the normalizing factor arbitrarily taken as $m_0 = 10,000\ kg$.

Another important factor considered in this formulation is the cross-sectional area, $A_k \in \mathbb{R}^+$, of the object. As reported in Rossi et al. (2017) and Rossi et al. (2022), this term is implemented considering its importance in the com-

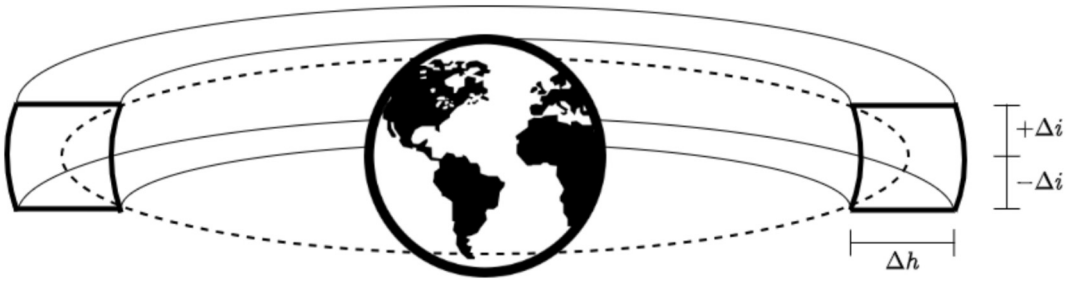

Fig. 1. A single toroidal region developing around a central circular orbit.

putation of the collision cross-section. The term is defined as follows:

$$\frac{A_k}{A_0} \tag{4}$$

where the normalizing term, $A_0 \in \mathbb{R}^+$, is set as $A_0 = 1\ m^2$.

Through the introduction of the cross-sectional area, it is possible to consider the trackability of the object, as proposed in Rossi et al. (2022), which would allow to include the current SST sensors' limitations in the criticality assessment.

For those analyses extending beyond the 7 day period after a break-up (as the process of detecting and consistently cataloguing the majority of the generated fragments typically requires several months, Klinner-Teo et al. (2026)), it is possible to include this contribution by considering the current SST limitations: objects with a characteristic length, say $d_c \in \mathbb{R}^+$, smaller than 10 cm (or equivalently, $Ak/A_0 < 0.0079\ m^2$) can be considered non-trackable. Therefore, following its original definition in Rossi et al. (2022), this term can be defined as:

$$\omega_k = \begin{cases} 1 & \text{if } d_c < 10 \text{ cm or } Ak/A_0 < 0.0079\ m^2 \\ 1 \cdot 10^{-4} & \text{if } d_c \geqslant 10 \text{ cm or } Ak/A_0 \geqslant 0.0079\ m^2 \end{cases} \tag{5}$$

where $\omega_k \in \mathbb{R}^+$, and the characteristic length can be computed as the diameter from the cross-sectional area by assuming circular shape for all objects.

For the subsequent simulations detailed in Sections 4 and 5, this contribution is set to unity, even if the characteristic length of the k-th object exceeds 10 cm. This simplification is necessitated by the fact that the available test cases lack information regarding the real objects' characteristic lengths; adopting this assumption ensures a fair comparison with the synthetic fragments.

3.2. Environmental term

The environment is considered in terms of the spatial density of objects larger than 10 cm at the average altitude of the considered satellite, $\rho(h) \in \mathbb{R}^+$. Values of density for each altitude interval, referred to the year 2030 and valid between 200 and 2000 km, are reported in Bombardelli et al. (2017), and this contribution can be computed as:

$$\frac{\rho_k(h)}{\rho_0} \tag{6}$$

where $\rho_k \in \mathbb{R}^+$ is the density at the altitude that the k-th object occupies at a given time instant, and ρ_0 is the normalizing factor, as the peak density value of MASTER-2009 population, equal to $\rho_0 = 6.8 \cdot 10^{-8}\ objects/km^3$.

It shall be specified that the referenced computation strategy is limited to the LEO, but an extension to higher orbital regimes could be achieved by retrieving the objects density at those altitudes following the methodology proposed in Bombardelli et al. (2017).

3.3. Residence time term

The final parameter considered is the residence time of the k-th object within the j-th toroid. This quantity introduces a geometrical and temporal consideration into the definition of the CNI, capturing the extent to which debris physically coexist with the satellite in its neighbourhood.

For each object, its orbital state is numerically propagated over a complete revolution using a finely discretised time grid, and all intermediate states at each time node $t_l \in \mathbb{R}^+$ (where $l \in \mathbb{N}^+$) are stored. Each intermediate position is then transformed from the ECI reference frame to the satellite's RTN frame. By defining the satellite's position and velocity at initial time as $\mathbf{r}_0$ and $\mathbf{v}_0$, respectively, this transformation is executed through Eq. 2.

The l-th transformed position vector, denoted as $\boldsymbol{r}_k(t_l) \in \mathbb{R}^3$ for conciseness, is used to compute both the radial distance from Earth's center, $r_k(t_l) \in \mathbb{R}^+$, and its elevation relative to the satellite's orbital plane, $el_k(t_l) \in \mathbb{R}$, according to the following equations:

$$r_k(t_l) = \sqrt{r_{k,x}^2(t_l) + r_{k,y}^2(t_l) + r_{k,z}^2(t_l)} \tag{7}$$

$$el_k(t_l) = \sin^{-1}\left(\frac{r_{k,z}(t_l)}{r_k(t_l)}\right) \tag{8}$$

Each pair is then evaluated against the geometric bounds of the j-th toroid by applying the following conditions:

$$R_{j,inner} \leqslant r_k(t_l) \leqslant R_{j,outer} \quad \text{and} \quad -\Delta i \leqslant el_k(t_l) \leqslant +\Delta i \tag{9}$$

where $\pm\Delta i$ defines the extent of the inclination range (i.e., the toroid' height) and $R_{j,inner}$ and $R_{j,outer} \in \mathbb{R}^+$ denote the inner and outer radial limits of the toroid, which can be computed as:

$$\begin{aligned} R_{j,inner} &= R_E + h_{min} + (j-1)\Delta h \quad \text{and} \quad R_{j,outer} \\ &= R_E + h_{min} + j\Delta h \end{aligned} \tag{10}$$

where $R_E \in \mathbb{R}^+$ and $h_{min} \in \mathbb{R}^+$ are the Earth's equatorial radius and minimum altitude selected for analyses, respectively. Conditions in Eq. 9 are checked at each time step and whenever both are satisfied the residence time is incremented by adding the corresponding time step.

The choice of the integration time step is of paramount importance. It must be sufficiently small to ensure that if the object's trajectory passes through the j-th toroid, at least one integration node falls within its bounds (i.e., its cross-section), as shown in Fig. 2. Concurrently, the step size must be selected considering the computational burden typically involved in these simulations, given the high number of objects to be propagated. In the present study, the adopted approach determines the integration time step by dividing the toroid's width by the maximum orbital velocity of the k-th fragment (i.e., the pericentre velocity). This strategy yields the maximum allowable time step required to guarantee that, should the k-th fragment traverse the

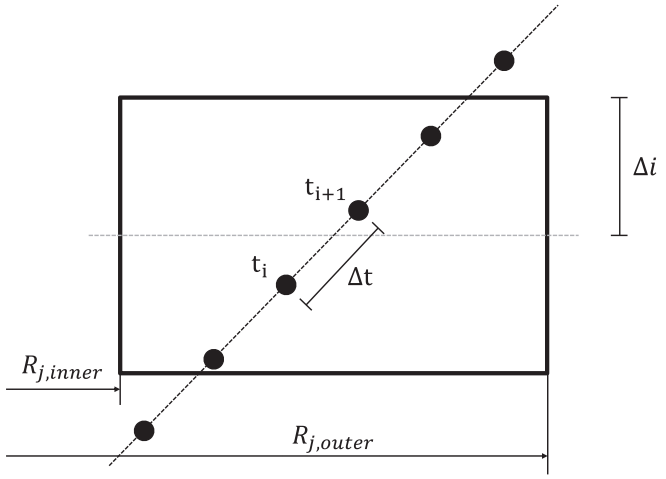

Fig. 2. Representation of integration time step impact in detecting object's passage through toroid cross-section.

j-th toroid, at least one temporal node is captured within its cross-section. Nevertheless, it must be noted that, because the Residence Time for each detected passage is approximated by summing the discrete time steps of the nodes located within the toroid, this method is inherently susceptible to over- or under-estimation. Indeed, reducing the time step would refine this estimate, at the cost of increasing the computational burden. Consequently, a discussion regarding the time step value is presented in Section 4.4.

Once the cumulative residence time, $\tau_{j,k} \in \mathbb{R}^+$, of the k-th object with respect to the j-th toroid is obtained, its contribution to the CNI is computed as:

$$\frac{\tau_{j,k}}{T_{sat}} \tag{11}$$

where $T_{sat} \in \mathbb{R}^+$ is the orbital period of the satellite under consideration.

3.4. Index definition

The overall criticality of the k-th object with respect to the j-th toroid, $CNI_{j,k} \in \mathbb{R}^+$, can be obtained by combining the previously defied terms into the CNI:

$$CNI_{j,k} = \frac{m_k}{m_0}\frac{A_k}{A_0}\frac{\rho_k}{\rho_0}\frac{\tau_{j,k}}{T_{sat}}\omega_{j,k} \tag{12}$$

The overall criticality of the j-th toroid, $CNI_j \in \mathbb{R}^+$, can be obtained as:

$$CNI_j = \sum_{k=1}^{M} CNI_{j,k} \tag{13}$$

where $M \in \mathbb{N}^+$ is the number of objects considered for the simulation. The overall procedure is summarized in Algorithm 1, where the various steps involved in computing the CNI are listed in order.

Algorithm 1. CNI Computation Algorithm

Require: Objects' states, masses, cross-sections
Propagate objects with high-fidelity over 7 days and exclude those having a final altitude lower than 250 km
for $k \in [1, M]$ ▷Loop over objects **do**
Propagate k-th object over its orbital period with two-body model with fine time grid $t = [0, T_{orb}]$
for $j \in [1, N]$ ▷Loop over toroids **do**
Compute $R_{j,inner}$ and $R_{j,outer}$ with Eq. 10
Compute the Mass Term from Eq. 3, m_k/m_0
Compute the Cross-Section, A_k/A_0, and Tracking Terms, ω_k, from Eqs. 4 and 5, respectively
Compute density at middle-point h_j between $R_{j,inner}$ and $R_{j,outer}$, and Environmental Term, $\rho_k(h_j)/\rho_0$, from Eq. 6
Compute rotation matrix from ECI to satellite's RTN frame with Eq. 1
Initialize Residence Time $\tau_{j,k} = 0$
for $l \in [2, length(t)]$ **do**
Rotate l-th state of object from ECI to satellite's RTN from Eq. 2
Compute radial distance $r_k(t(l))$ and elevation $el_k(t(l))$ from Eqs. 7 and 8
if $R_{j,inner} \leqslant r_k(t(l)) \leqslant R_{j,outer}$ **then**
if $-\Delta i \leqslant el_k(t(l)) \leqslant +\Delta i$ **then**
$\tau_{j,k} = \tau_{j,k} + (t(l) - t(l-1))$
end if
end if
end for
Compute the Residence Time Term, $\tau_{j,k}/T_{sat}$, from Eq. 11
Compute k-th object's contribute on j-th shell CNI, $CNI_{j,k}$, from Eq. 12
end for
end for
Compute total CNI on each shell, CNI_j, by summing all $CNI_{j,k}$ over k from Eq. 13

4. Test Case 1: COSMOS 1404

The approach introduced is evaluated with the real-world case of COSMOS 1408, a satellite taken down by Anti-SATellite (ASAT) weapon system on November 15, 2021 (Pardini and Anselmo, 2023).

Initially, the satellite's fragmentation is modelled using the NASA Standard Break-up Model (SBM), a tool created and utilized within NASA's EVOLVE 4.0 orbital debris model in 2001 and described in Johnson et al. (2001). This tool employs empirical relationships retrieved from laboratory experiments and observations of break-up events occurring in space. The SBM encompasses three

main components: size distributions, area-to-mass distributions, and ΔV distributions. Each of these components is dependent on at least another one to achieve thorough event modelling and is further tailored to specific event types, such as explosions or collisions.

Afterwards, a pre-processing is applied on these synthetic fragments by preliminarily propagating them for 7 days with the high-fidelity propagator described in Morselli et al. (2014), considering the gravitational perturbation due to J_2 effect and the atmospheric drag. The objective is to discard any object that re-enters the Earth's atmosphere during this time span, whereas the surviving ones are retained for CNI computation.

Subsequently, the Two-Line Elements (TLE) s provided by the Italian Air Force, derived from observations conducted a few hours after the COSMOS 1408 event, are propagated backwards from their reference epochs to the precise time of the event reported in the literature, after which the CNI algorithm is applied. This facilitates a comparison between the criticality of the toroids simulated through NASA SBM synthetic fragments and the criticality of the observed ones, thereby assessing the predictive capabilities of the proposed approach.

In the final phase of the analysis, a conjunction screening is performed between fictitious assets, placed in circular orbits coincident with the centreline of each toroid, and both synthetic and real fragments. The objective is to determine whether the toroids' CNI levels can provide a high-level estimate of the potential number of conjunctions, and their spatial distribution, encountered while operating within the vicinity of the debris cloud. Importantly, the proposed CNI technique is not intended to replace a comprehensive conjunction screening process. Rather, it serves as a means to qualitatively evaluate the dangerousness of the orbital environment surrounding an asset without necessitating computationally intensive simulations, particularly in scenarios where complete and accurate information regarding newly formed debris are still being gathered.

As a final note about the successive simulations, the algorithms are run on 13th Gen Intel(R) Core(TM) i7-1370P @1.90 GHz, 14 cores, 20 logical processors, and using Matlab 2024a.

Table 1
NASA SBM input and orbital data for COSMOS 1408 ASAT event.

Parameter	Value	Unit
Primary Mass	1750	kg
Projectile Mass	63.5	kg
Impact Velocity	4.6	km/s
Sizes Range	0.1–1	m
Pericentre Altitude	453	km
Apocentre Altitude	489	km
Inclination	82.9	deg
Right Ascension	123.4	deg
Argument of Pericentre	91.92	deg
True Anomaly	341.85	deg

4.1. Synthetic fragments generation

To simulate the debris cloud generated from COSMOS 1408 through NASA SBM, specific data about the satellite and the event are employed. The estimated mass of COSMOS 1408 is 1750 kg, as noted by Smith et al. (2024), and the mass of the ASAT projectile is 63.5 kg. Within the SBM, the "collision" model is applied, with the lower and upper bounds of the fragment size set to 10 cm and 1 m, respectively; resulting in 1434 fragments in total (which complies with the order of magnitude found in literature, LeoLabs (2021); Grattagliano et al. (2025)). As TLE regarding the real fragments cover objects down to 10 cm, such limit is also applied to the synthetic ones (even if SBM can produce millimetre-class fragments) in order to have a fair comparison between real and simulated populations.

The collision's impact velocity is set at 4.6 km/s (Smith et al., 2024; Pardini and Anselmo, 2023), and the initial orbit of the debris cloud matches that of the COSMOS satellite retrieved from catalogue data just before the event and summarized in Table 1. Regarding the actual fragments' TLEs, the event epoch is found in literature as 15th November 2021 at 02:47:59 UTC, from study in Muciaccia et al. (2024).

Fig. 3 depicts the SBM generated and the TLE-based clouds, where the latter exhibits a cross-shape distribution and a clockwise shift in the right-ascension of the ascending

(a) (b)

Fig. 3. COSMOS 1408 synthetic (a) and real fragments from TLE (b) representation after 7 days from event date in ECI reference frame.

node. This discrepancy is to be attributed to the way SBM models fragments' ΔV magnitude through a bi-variate normal distribution with empirically derived parameters, and to the adopted assumption of isotropic distribution on the fragment's direction. Additionally, discrepancies between the SBM and the actual event are anticipated, as the projectile and impact velocity details are inferred through various studies without confirmation by official sources. According to NASA's SBM, the parameters currently in use indicate an impact energy per mass of 383.9 J/g, notably exceeding the catastrophic collision classification threshold of 40 J/g, implying that the NASA SBM might inadequately model the event's complexity, a conclusion also drawn by Olivieri et al. (2024). Ultimately, Fig. 4 presents the Gabbard plots for debris generation comparison. The plots of semi-major axes against pericentre and apocentre altitudes for both clouds indicate compatible spreading, highlighting that the altitude distribution is accurately replicated.

4.2. Toroids criticality with synthetic and real fragments

In evaluating the criticality of toroids, a fundamental decision involves selecting the range of altitudes for the analyses and the altitude discretization. These parameters are crucial as they determine the analysis resolution and affect the computational time. While a finer discretization enhances the detail in depicting fragments' impact at varying altitudes, the number of calculations required approximately increases linearly with the number of toroids specified.

In this study, the altitudes range is arbitrarily selected to be between 420 km and 550 km, ensuring comprehensive coverage of the COSMOS 1408's entire orbit, along with adjacent altitudes. This specific range is chosen to be subdivided into 40 toroidal regions, each having a cross-section width of 3.25 km. The inclination range, which translates into the toroids' height, is determined based on this altitude width, thereby achieving an almost-square cross-sectional shape. Consequently, each toroid has a height of 3.25 km and spans an inclination from −0.0135 degrees to + 0.0135 degrees relative to the asset's orbital plane in the RTN frame, as discussed in Section 3.3.

Fig. 5(a) depicts the criticality of each toroid due to the COSMOS 1408 synthetic fragments created through the NASA SBM and placed at the position of the parent's orbit, while Fig. 5(b) proposes the same plot in heatmap format to provide a more graphically insightful representation of the toroids concept.

As expected, the criticality shows two peaks, the first one taking place in the vicinity of the event's pericentre, where most of the produced fragments settled in the 7 days after the event and return periodically. A second peak, reaching the highest criticality level, is located around 510 km altitude. An interesting aspect to consider is their

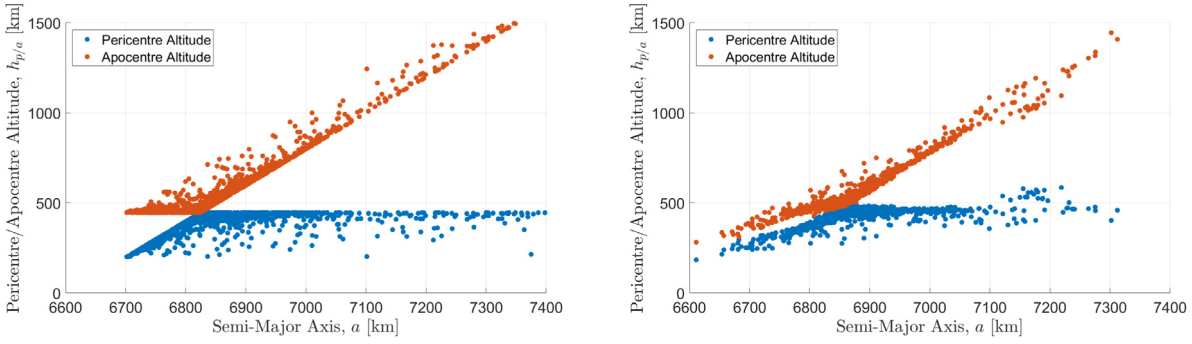

(a) (b)

Fig. 4. COSMOS 1408 synthetic (a) and real fragments from TLE (b) Gabbard plots of semi-major axes against pericentre and apocentre altitudes.

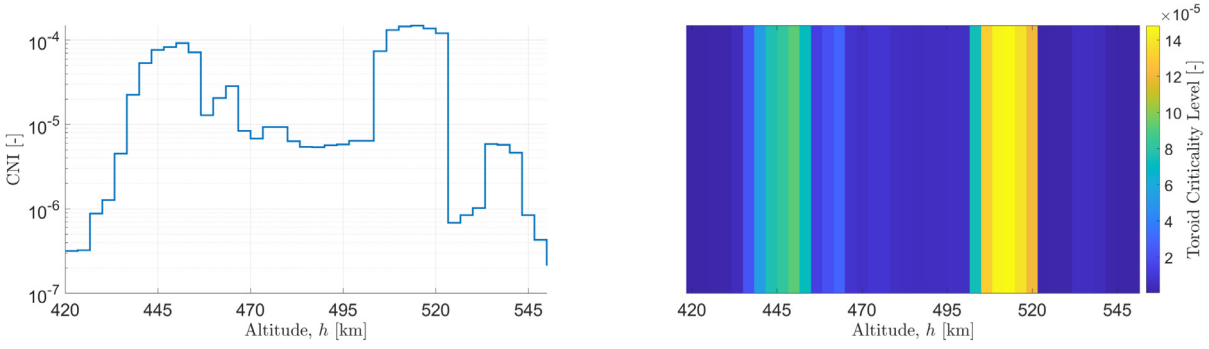

(a) (b)

Fig. 5. COSMOS 1408 toroids' criticality profile (a) and heatmap (b) through CNI after 7 days from event epoch with synthetic fragments.

different natures, as the former is mainly due to the Residence Time term which has a spike slightly below event's altitude, as observable in Fig. 6(a), while the latter is given by the spatial density in the Environmental Term, which reaches its peak (in the selected altitudes interval) between 502 km and 550 km, as depicted in Fig. 6(b).

In general, the criticality is strongly dictated by the SBM produced ΔV distribution, the atmospheric density during propagations and the simulation time after event. If a longer than 7 days time window was to be considered, some debris would start to decay in atmosphere with a rate dependent on each fragment's ballistic coefficient and atmospheric density at the altitude. This would imply lower fragments considered in the CNI and possible shifting of the criticality profile peak to lower altitudes (as elliptical orbits, under drag, start to circularize and then decay in time).

To assess the capabilities of the proposed method, the TLE of 904 real fragments from COSMOS 1408 are used to compute the toroids' criticality 7 days after the breakup. The main limitation in this case is the absence of information on both the masses and characteristic lengths of the objects; consequently, the corresponding CNI terms are set to unity for these simulations. Figs. 7(a) and 7(b) show the CNI level of each toroid resulting from the real fragments. By comparing the CNI levels of the two datasets, it is immediately apparent that, although real fragments exhibit a broader distribution shifted towards higher values with respect to the synthetic ones, the criticality in Fig. 5 shows a similar peak above 500 km. The difference in order of magnitude between the two cases can be attributed to the lack of mass and cross-sectional area data for the real fragments, which necessitates setting the corresponding CNI terms to unity. (see Fig. 8).

4.3. Conjunction analysis with fragments

The main challenge in using such an index as an hazard indicator lies in the lack of a definitive safety threshold that determines when a toroid becomes excessively dangerous, necessitating temporary relocation of an asset. Various threshold definitions can be considered; however, this study prefers to avoid specifying a criticality level and instead employs a conjunction screening approach to assess if CNI values accurately represent potential conjunctions. The idea is that, rather than conducting conjunction screenings individually for each toroid and each fragment since the beginning, a task that could be computationally time-consuming, an operator can determine the CNI using synthetic fragments, incorporate this into the reference criticality levels, and then decide whether to move an asset directly or refine simulations with a conjunction screening. This aspect of computational efficiency is particularly crucial when considering that satellite operators are required to monitor several satellites simultaneously.

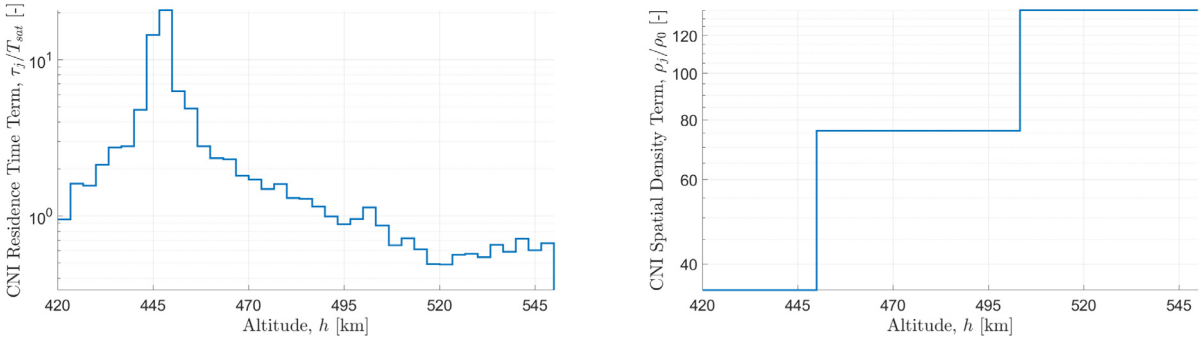

Fig. 6. COSMOS 1408 toroids' Residence Time (a) and Environmental (b) terms after 7 days from event epoch with synthetic fragments.

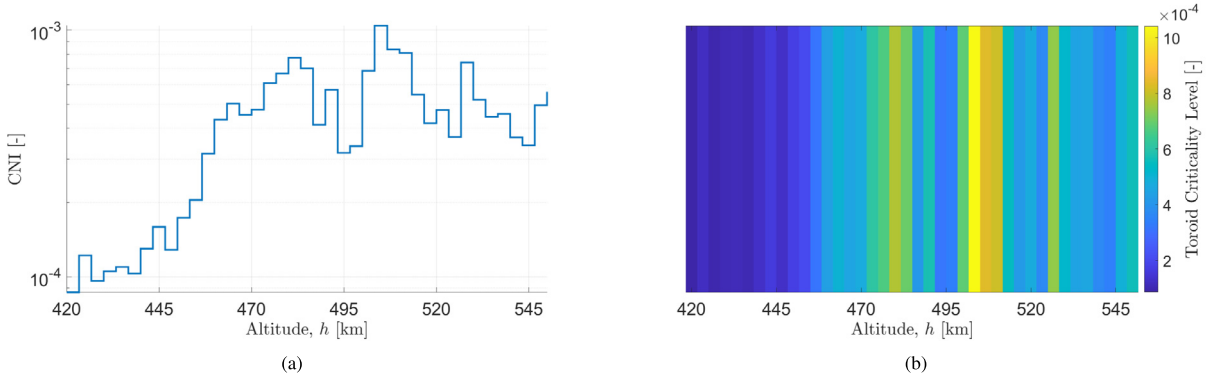

Fig. 7. COSMOS 1408 toroids' criticality profile (a) and heatmap (b) through CNI after 7 days from event epoch with real fragments.

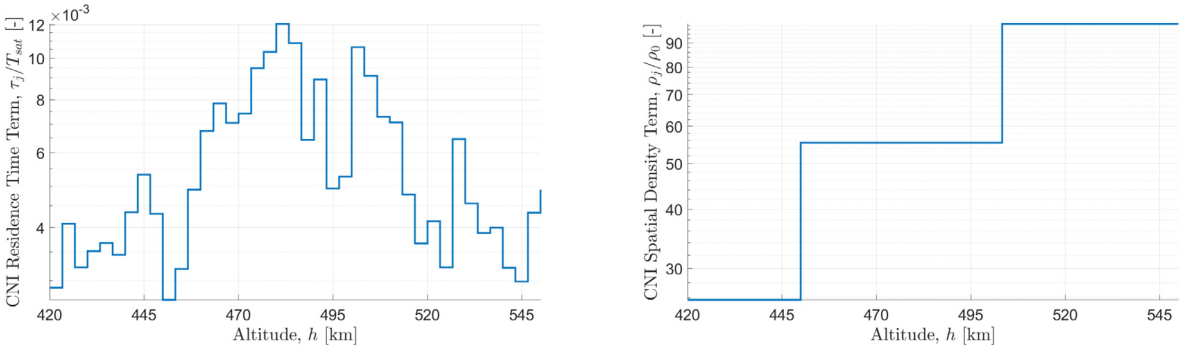

(a) (b)

Fig. 8. COSMOS 1408 toroids' Residence Time (a) and Environmental (b) terms after 7 days from event epoch with real fragments.

To identify potential close encounters, each fragment and the satellite under investigation are propagated using a sufficiently fine temporal grid. For each k-th fragment–satellite pair, the relative position, $\mathbf{r}_{rel}(t_l) \in \mathbb{R}^3$, and relative velocity, $\mathbf{v}_{rel}(t_l) \in \mathbb{R}^3$, are evaluated at each discrete time instant $t_l \in \mathbb{R}^+$. The scalar product between these vectors is then computed at each time step, and a potential close encounter is identified whenever the following condition is satisfied:

$$\mathbf{r}_{rel}(t_l) \cdot \mathbf{v}_{rel}(t_l) = 0. \tag{14}$$

This quantity is negative when the two objects are approaching and positive when they are receding. Consequently, the temporal evolution of the scalar product is provided to a nonlinear zero-finding algorithm to determine the time instant at which the condition is satisfied. At this time, the norm of the relative position vector is compared against the prescribed Miss Distance (MD); if it is less than or equal to this threshold, the event is classified as a conjunction.

For the present simulations, the circular "central orbit" of each toroid is considered as a fictitious asset to determine close approaches with the fragments. To this end, the MD is adopted as the only safety metric, given its simplicity and the absence of uncertainties information, especially for synthetic fragments. Such a screening is performed in a time span from the event epoch to 7 days later.

Fig. 9 shows the number of close approaches for each toroid with synthetic fragments, exceeding the threshold MD of 0.5, 1.5, 3.5 and 5 km. Similarly, Fig. 10 shows

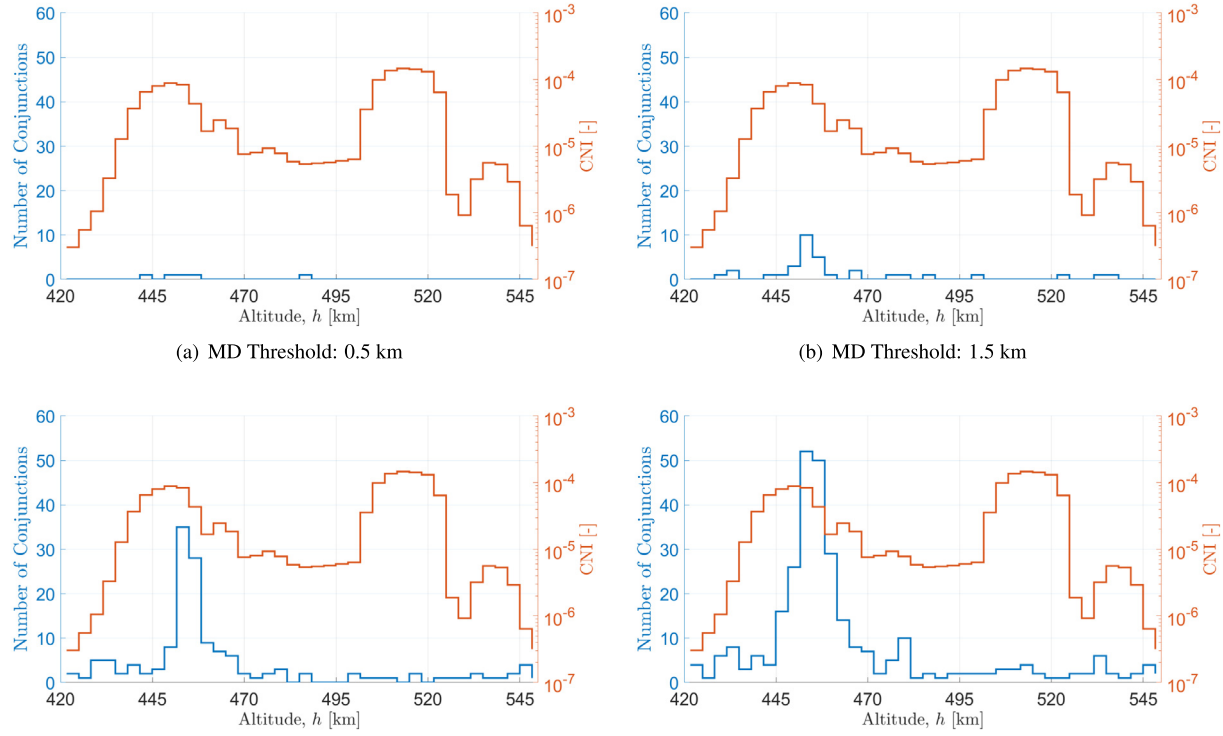

(a) MD Threshold: 0.5 km (b) MD Threshold: 1.5 km

(c) MD Threshold: 3.5 km (d) MD Threshold: 5 km

Fig. 9. Number of conjunctions between toroids and synthetic fragments of COSMOS 1408 exceeding the 0.5 km (a), 1.5 km (b), 3.5 km (c) and 5 km (d) MD threshold in 7-day period, and CNI increase with respect to reference.

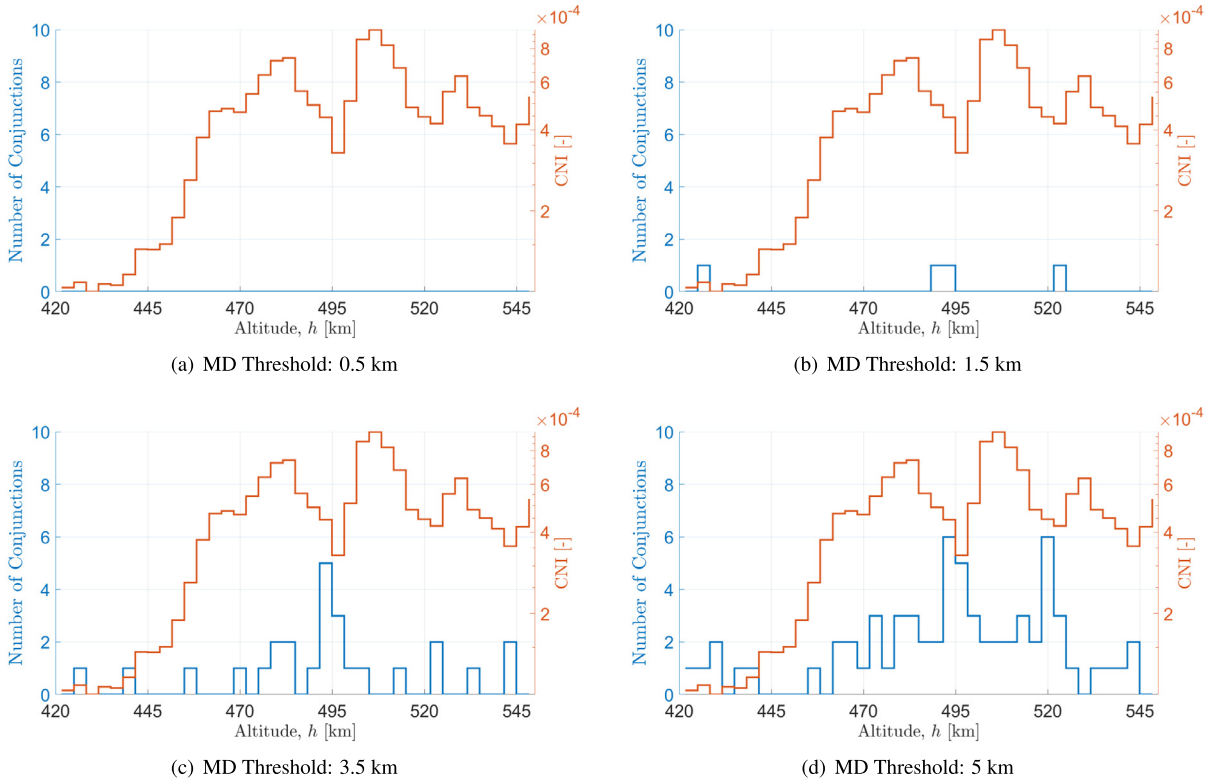

(a) MD Threshold: 0.5 km

(b) MD Threshold: 1.5 km

(c) MD Threshold: 3.5 km

(d) MD Threshold: 5 km

Fig. 10. Number of conjunctions between toroids and real fragments of COSMOS 1408 exceeding the 0.5 km (a), 1.5 km (b), 3.5 km (c) and 5 km (d) MD threshold in 7-day period, and CNI increase with respect to reference.

the number of close approaches for each toroid with the real fragments from the TLEs, employing the same MD thresholds.

At first, it is possible to observe that the maximum number of conjunctions with synthetic fragments is largely overestimated by one order of magnitude with respect to the real case, where the former predicted about 53 close encounters while the latter showed only 6. However, the critical point is the difference in their distributions, considering that synthetic scenario shows a peak close to the event's altitude of 456.25 km, while real fragments have two peaks at 491.75 km and 520 km altitude. Nevertheless, the second synthetic fragments' CNI peak corresponds to a number of conjunctions comparable with respect to real ones'.

From this last analysis, it is possible to understand that the CNI allows to obtain a high-level indication of the hazard posed by newly formed fragments to an asset without needing long and complex computations of the whole population, a conclusion also drawn by authors in Rossi et al. (2022).

4.4. Computational efficiency assessment

As previously stated, the present technique is developed with computational efficiency as the primary driver. To assess such efficiency, the synthetic fragments associated with the COSMOS 1408 event are analysed. As outlined in Algorithm 1, during each iteration, the algorithm propagates the k-th fragment for a single orbital period; this propagation employs Keplerian dynamics and the Adams–Bashforth-Moulton integrator of variable order 1 to 13 with both absolute and relative tolerances of 10^{-13}, considering a fixed time step computed as described in Section 3.3.

Fig. 11(a) illustrates the probability density function of the CPU time required for the CNI computation per fragment. This computational time encompasses both the fixed time step Keplerian propagation and the calculation of the fragment's CNI contribution to each of the 40 toroids. The results depicted show the distribution of the CPU times falling between the 5th and 95th percentiles.

It can be observed that the average computational time per fragment is 0.33 s, with the numerical integrator accounting for the majority of this duration. These times are obtained with the broadest time step possible, dt_{max}, which reduces the number of integration steps, but could lead to an inaccurate estimation of the Residence Time term. For this reason, Fig. 11(b) presents a box plot of the required CPU times, wherein the maximum allowable time step is progressively reduced to evaluate how the computational cost scales with a finer time grid.

It is important to notice that such performances were obtained with toroids of 3.25 km width which, following the computation method explained in Section 3.3, leads to an average time step below 0.5 s. However, as the time step is directly linked to the toroid's size, using smaller cross-sections would increase the computational cost.

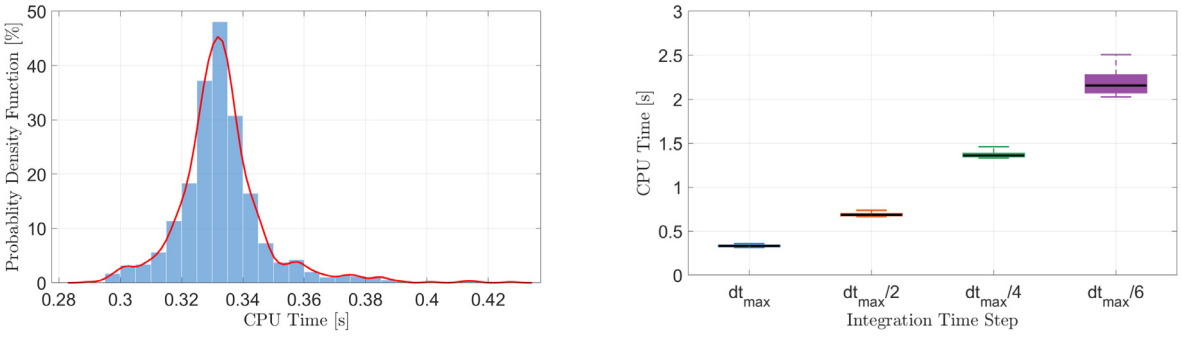

(a) (b)

Fig. 11. Probability density function (a) and box plot (b) of the CPU time required per iteration of the for-loop in Algorithm 1, considering the maximum allowable time step dt_{max} (a) and four time step options (b), Keplerian dynamics and the Adams–Bashforth-Moulton integrator of variable order 1 to 13 with both absolute and relative tolerances of 10^{-13}, and outliers rejection to the 5th and 9.5th percentiles.

4.5. Sensitivity analyses

As previously discussed regarding the selection of the fixed integration time step, the maximum allowable value is defined as the toroid's radial width divided by the k-th fragment's maximum orbital velocity (i.e., its pericentre velocity). However, employing this upper limit can inherently lead to an over- or under-estimation of the Residence Time term. To quantify this effect, Fig. 12 adopts $dt_{max}/6$ as a reference baseline to illustrate the discrepancies introduced in each toroid when the time step is increased to $dt_{max}/4, dt_{max}/2$, and dt_{max}.

The analysis reveals that the relative errors remain predominantly below $\pm 0.1\%$, with the maximum value occurring when t_{max} is directly employed as the integration time step. Conversely, the performance metric presented in Fig. 11(b) demonstrates that the computational cost scales exponentially with each successive refinement of the temporal grid. It can be concluded that adopting a time step of $t_{max}/2$ effectively mitigates the computational burden while significantly reducing the errors compared to the baseline t_{max}.

A final analysis investigates the sensitivity of the CNI with respect to the number of toroids, a parameter that, as previously demonstrated, directly dictates both the toroid width and the integration time step, which in turns affects the computational burden. In Fig. 13, the CNI profile for the COSMOS 1408 synthetic fragments is depicted using a varying number of toroids, from 10 to 100 (corresponding to a toroid width from 13 to 1.3 km), within the same altitude range. As can be observed, increasing the number of toroids yields to an overall CNI magnitude decrease by one or more orders of magnitude. Increasing the number of toroids, while keeping constant the altitudes range, narrows the toroids' cross-sections, which in turn facilitates a more precise estimation of the Residence Time term. Consequently, the spatial resolution of the distribution is significantly enhanced, revealing in greater detail how specific altitude bands are affected.

5. Test Case 2: IRIDIUM 33 - COSMOS 2251

To further evaluate the capabilities of the proposed methodology, the collision between IRIDIUM 33 and COSMOS 2251, which occurred on 10th February 2009 (Pardini and Anselmo, 2011; Kelso, 2009), is selected as the second test case. The former was an operational US communications satellite, while the latter was a long-defunct Russian communications satellite. Notably, this event marked the first time since the inception of human

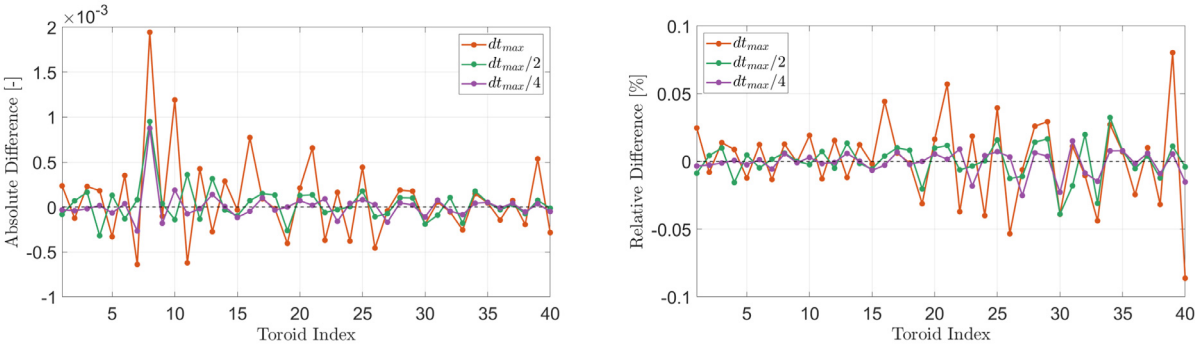

(a) (b)

Fig. 12. Absolute (a) and relative (b) differences in computing the total Residence Time term of each toroid, comparing a reference fixed time step of $dt_{max}/6$ against time steps of $dt_{max}, dt_{max}/2$, and $dt_{max}/4$.

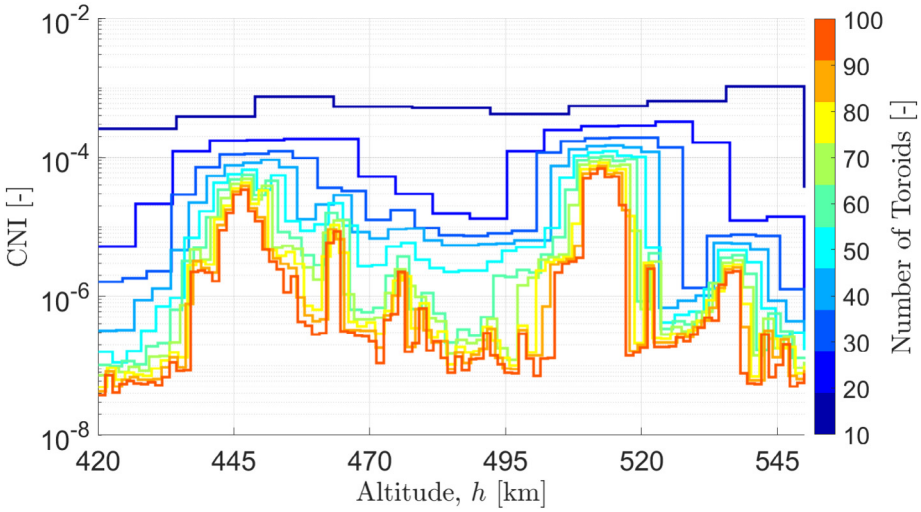

Fig. 13. COSMOS 1408 toroids' criticality profile through CNI after 7 days from event epoch with synthetic fragments using different numbers of toroids, from 10 to 100 toroids, and always employing the maximum time step.

spaceflight that two intact satellites collided in orbit (Kelso, 2009). The analysis follows the same procedure detailed in Section 4.

5.1. Synthetic fragments generation

The mass of IRIDIUM 33 is reported as 556 kg, whereas the mass of COSMOS 2251 is estimated at approximately 900 kg (Kelso, 2009; Pardini and Anselmo, 2011). Within the SBM, the "collision" model is applied, with the lower and upper bounds for fragments size set to 10 cm and 1 m, respectively. This configuration generates a total of 1209 fragments, which is compliant with the order of magnitude reported in the literature (Kelso, 2009; Olivieri et al., 2024). Given that the TLE data for the actual fragments only cover objects down to 10 cm, this threshold is identically applied to the synthetic fragments to ensure a fair comparison between the observed and simulated populations.

The impact velocity of the collision is estimated to be 11.6 km/s (Frey and Colombo, 2021; Pardini and Anselmo, 2011), and the orbits of the parents are retrieved from literature (Pardini and Anselmo, 2011; Frey and Colombo, 2021) and catalogue data immediately prior to the event and summarised in Table 2. Finally, regarding the actual fragments', 402 objects' TLEs close to the event epoch, established in the literature as 10th February 2009 at 16:55:59.8 UTC (Kelso, 2009), are obtained from the SpaceTrack database.

Table 2
Estimated mass and orbital data for IRIDIUM 33 - COSMOS 2251 collision event.

Parameter	IRIDIUM 33	COSMOS 2251	Unit
Estimated Mass	556	900	kg
Pericentre Altitude	779	784	km
Apocentre Altitude	808	826	km
Inclination	86.4	74.0	deg
Right Ascension	121.7	19.5	deg
Argument of Pericentre	85.1	98.7	deg
True Anomaly	274.9	358.6	deg

As before, to validate the generated fragment cloud, Fig. 14 presents the Gabbard diagrams for both the synthetic and real fragments (derived from TLEs) associated with the collision, plotting the semi-major axes against the pericentre and apocentre altitudes. With respect to the previous test case, for this break-up the NASA SBM reproduces with higher accuracy the fragments distribution.

5.2. Toroids criticality with synthetic and real fragments

For this test case, the altitudes range is selected to be between 730 km and 860 km, ensuring comprehensive coverage of both IRIDIUM 33 and COSMOS 2251's entire orbits, along with adjacent altitudes. In order to preserve the same scales employed for the COSMOS 1408 case, this specific range is chosen to be subdivided into 40 toroidal regions, each having a cross-section width of 3.25 km. The inclination range, which translates into the toroids' height, is determined based on this altitude width, thereby achieving an almost-square cross-sectional shape.

It is evident that, despite some distributional discrepancies, the CNI profiles depicted in Figs. 15 and 17 exhibit significantly greater similarity than in the first test case. The synthetic and real criticality peaks differ by only 6.5 km, and the overall profile is reproduced more accurately than in the previous analysis. This improved alignment is primarily attributable to the SBM's more accurate modelling of this specific scenario, which more closely aligns with the model's underlying statistical characteristics. However, it must also be noted that the two distributions are an order of magnitude apart. This discrepancy is due to the differing number of objects comprising the synthetic and real clouds, an effect that can also be observed in the Residence Time and Environmental

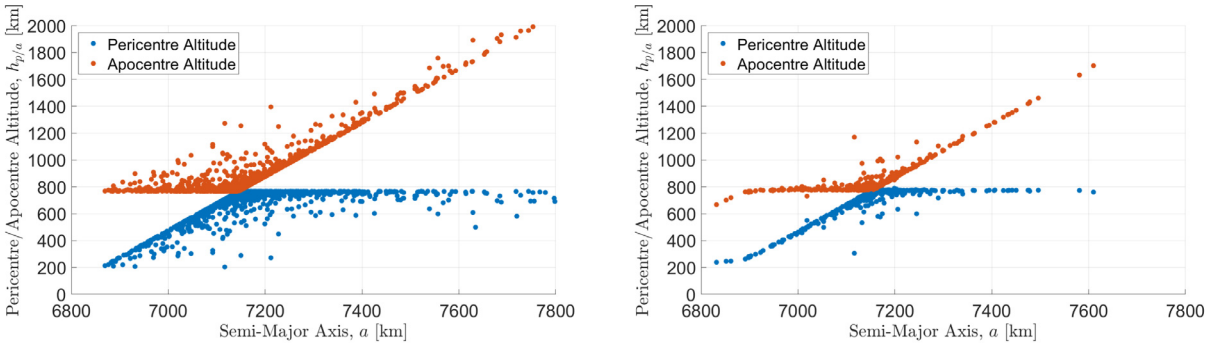

Fig. 14. IRIDIUM 33-COSMOS 2251 synthetic (a) and real fragments from TLE (b) Gabbard plots of semi-major axes against pericentre and apocentre altitudes.

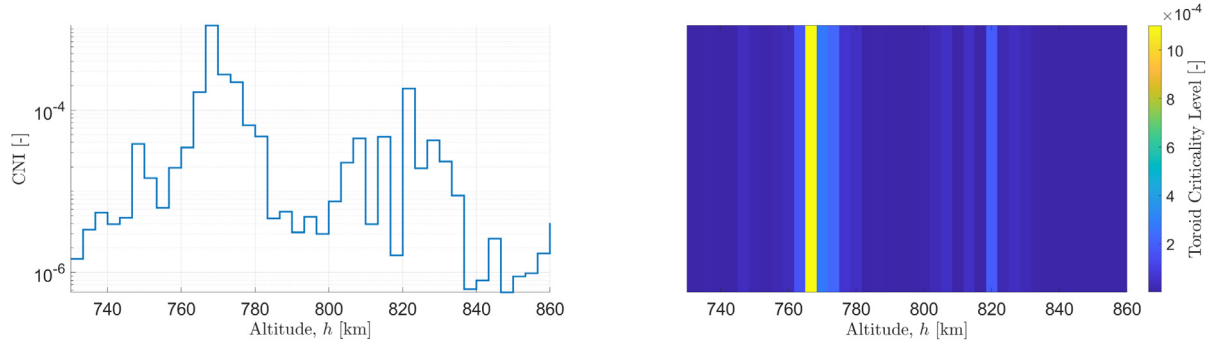

Fig. 15. IRIDIUM 33-COSMOS 2251 toroids' criticality profile (a) and heatmap (b) through CNI after 7 days from event epoch with synthetic fragments.

terms depicted in Figs. 16 and 18. In fact, within the Space-Track database, of the various fragments catalogued since this collision took place, in the vicinity of the estimated epoch only 402 fragments resulted to be employable for the simulations. This disparity leads to a substantial difference in the objects distributions, which subsequently affected the magnitude of the CNI across the toroids.

5.3. Conjunction analysis with fragments

Following the procedure detailed in Section 4.3, a conjunction screening is also applied to this test case to determine whether there is any correlation between the number of potential conjunctions and the criticality peaks within the toroids.

Fig. 19 illustrates the number of close approaches within each toroid for the synthetic fragments, evaluated against threshold MD values of 0.5, 1.5, 3.5, and 5 km. Similarly, Fig. 20 presents the number of close approaches per toroid involving the actual fragments derived from the TLEs, employing identical MD thresholds.

As can be observed in both the synthetic and actual cases, the number of conjunctions appears to follow the CNI profile, exhibiting peaks in the vicinity of the critical-

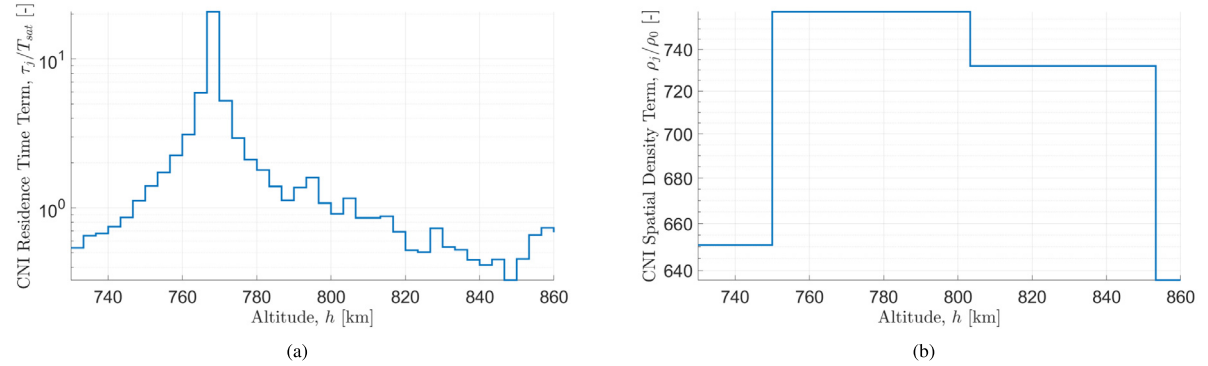

Fig. 16. IRIDIUM 33-COSMOS 2251 toroids' Residence Time (a) and Environmental (b) terms after 7 days from event epoch with synthetic fragments.

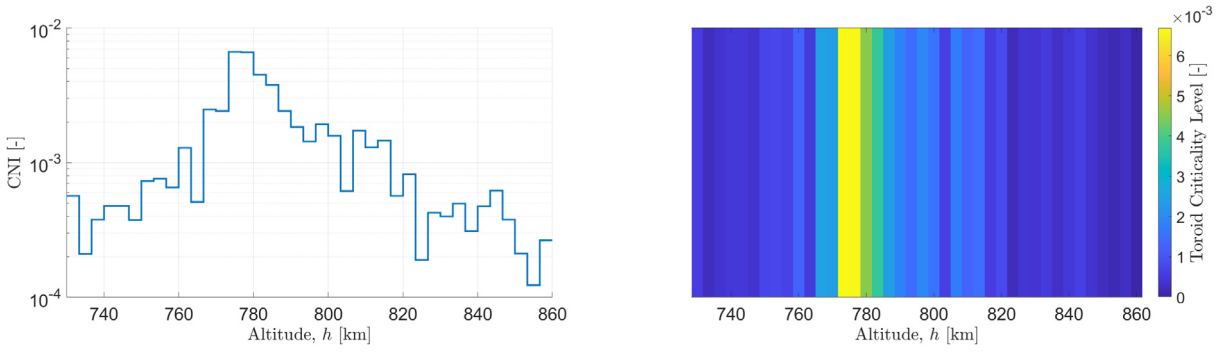

(a) (b)

Fig. 17. IRIDIUM 33-COSMOS 2251 toroids' criticality profile (a) and heatmap (b) through CNI after 7 days from event epoch with real fragments.

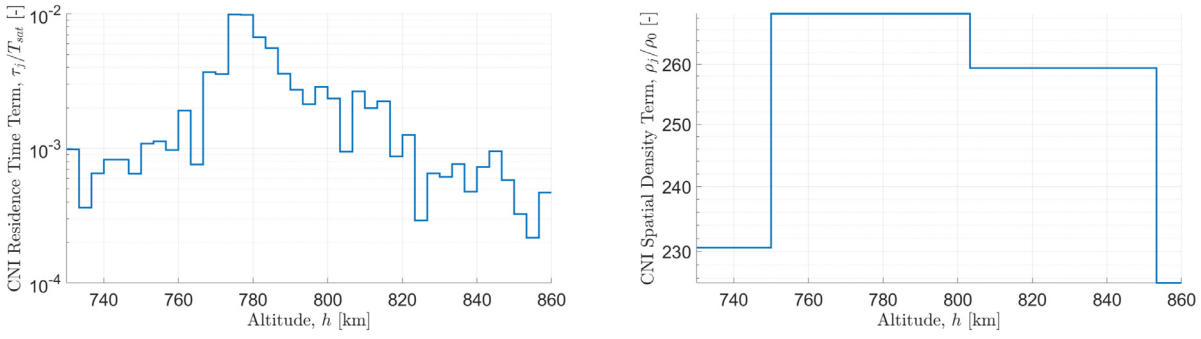

(a) (b)

Fig. 18. IRIDIUM 33-COSMOS 2251 toroids' Residence Time (a) and Environmental (b) terms after 7 days from event epoch with real fragments.

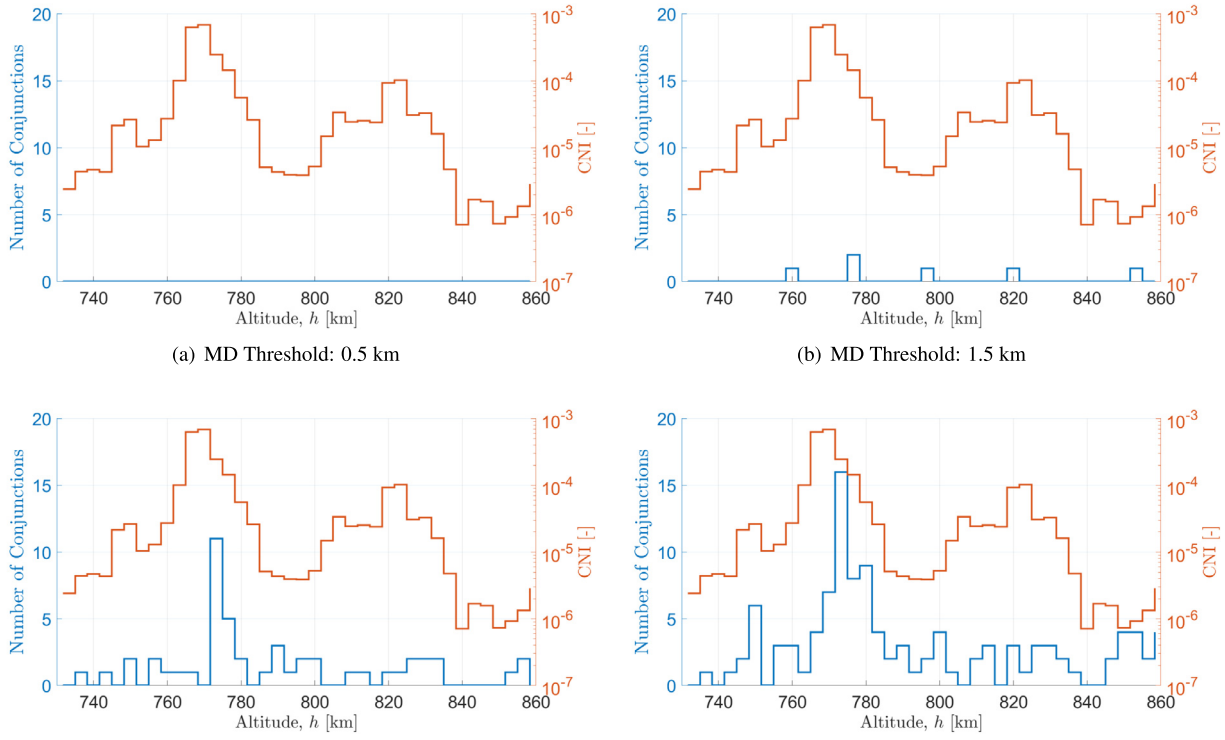

(a) MD Threshold: 0.5 km (b) MD Threshold: 1.5 km

(c) MD Threshold: 3.5 km (d) MD Threshold: 5 km

Fig. 19. Number of conjunctions between toroids and synthetic fragments of IRIDIUM 33-COSMOS 2251 exceeding the 0.5 km (a), 1.5 km (b), 3.5 km (c) and 5 km (d) MD threshold in 7-day period, and CNI increase with respect to reference.

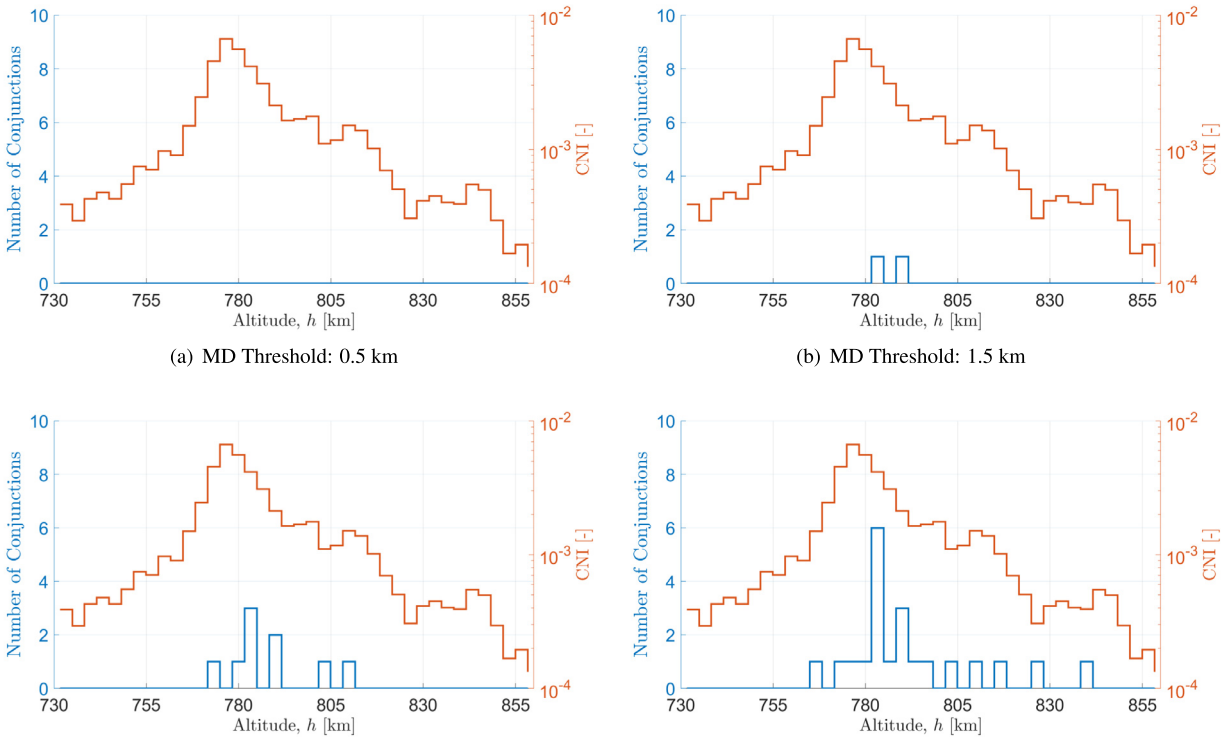

(a) MD Threshold: 0.5 km

(b) MD Threshold: 1.5 km

(c) MD Threshold: 3.5 km

(d) MD Threshold: 5 km

Fig. 20. Number of conjunctions between toroids and real fragments of IRIDIUM 33-COSMOS 2251 exceeding the 0.5 km (a), 1.5 km (b), 3.5 km (c) and 5 km (d) MD threshold in 7-day period, and CNI increase with respect to reference.

ity maxima. Similar to the CNI levels themselves, the discrepancy in magnitude between the two cases can be directly attributed to the differing number of objects comprising each distribution.

6. Conclusions and future developments

This work presented the Criticality of Neighbourhood Index (CNI), an index for assessing the environmental impact of break-up events on the neighbouring region of a specific asset. The proposed method identifies the most critical regions influenced by newly generated fragments without requiring complex and time-consuming conjunction screenings. Despite the need for propagation to compute the Residence Time term, previously solved analytically in the original CSI and Shell Criticality formulations (which were designed for long-term analyses using spherical shell domains), the method computes the overall criticality of a toroidal volume in a few seconds. This level of efficiency is consistent with its intended use, namely rapid post-event assessment to promptly support decisions on whether an asset should be manoeuvred to a different orbit.

To benchmark the predictive capabilities of the algorithm, two test cases were considered. Initially, the TLEs for 904 fragments produced by the COSMOS 1408 event, close to the event's epoch, were available and selected as the first test case. As demonstrated, due to the inherent difficulties in reproducing this specific scenario using the NASA SBM, the results exhibited only a marginal resemblance between the CNI profiles computed with synthetic and real fragments. Consequently, the collision between IRIDIUM 33 and COSMOS 2251 was selected as a second test case, for which 402 TLEs were retrieved from the SpaceTrack database. In this instance, despite discrepancies in the CNI magnitude arising from the differing number of fragments, the criticality distributions demonstrated a significantly higher degree of similarity.

Regarding its limitations, the method relies on the assumption of circular orbits for the screened asset. The current formulation leverages symmetry to describe toroidal volumes through simple inequality conditions, which is valid for circular cases. However, while circular orbits are prevalent in LEO, this assumption restricts applicability. If an elliptical orbit was to be considered with current formulation, portion of its path would end up outside the toroid's volume, rendering the criticality assessment not applicable to its entirety. Therefore, a more general geometric representation of the toroidal domains should be investigated to account for elliptical orbits and also different cross-sectional shapes. Regarding this second point, in this study a square section was adopted, however another possible choice could be the specific satellite's covariance ellipsoid's radii as width and height, in this way the toroid volume would fully contain the covariance cross-section and account also for position uncertainties.

Furthermore, the influence of the high-fidelity propagator employed for the pre-processing of the synthetic fragments needs some considerations. In subsequent research, a comparative performance assessment of various propagators should be conducted to evaluate their respective impacts on the evolution of the fragment cloud, while identifying the model that also minimises the computational burden. Indeed, within the current pipeline, the most time-consuming phase is the pre-processing of synthetic fragments. This step must be optimised to enhance the overall procedural efficiency, an aspect of paramount importance given its intended field of application.

Finally, the definition of a safety threshold, namely a CNI value above which an asset should be advised to temporarily relocate to a different altitude, represents an additional need in future researches. The challenge of establishing a criticality threshold has remained largely unaddressed in the literature, despite the various formulations and iterations of the original Criticality Index. During the research on the CNI, several methodologies were explored to tackle this gap. However, it was consistently concluded that the investigated approaches failed to establish a robust correlation between CNI levels and the actual risk of collisions. The main challenge lies in the strong sensitivity of results to parameters such as propagation window discretization and normalization coefficients, which render a generalization of the index levels cumbersome. Ultimately, conjunction screening based on miss distance yielded the most promising results, having peaks in the number of detected conjunctions close to the peaks in the CNI profile. For future studies, a comprehensive statistical analysis should be conducted, utilising data from various actual fragmentation events across different orbital regimes. Subsequently, increments in the CNI relative to nominal levels could be correlated with metrics such as the cumulative probability of collision or variations in the expected annual number of collision avoidance manoeuvres. This correlation would facilitate the definition of specific CNI thresholds indicating that remaining on the nominal orbit could be operationally unacceptable.

Declaration of competing interest

The authors declare that they have no known competing financial interests or personal relationships that could have appeared to influence the work reported in this paper.

Acknowledgments

The presented research was performed in the framework of the project *Autonomous Space-based Situational Awareness and Artificial Intelligence* (ASSAI), EDA Contract No. B PRJ-RT-1175. The authors would like to thank Cap. Giuseppe Pariti of Italian Air Force for supplying the real fragments TLEs and the insightful data about the break-up event.

The authors also extend their gratitude to Marco Felice Montaruli and Paola Grattagliano for their significant contributions to the code development employed in the simulations discussed in Section 4.1, as well as for their indispensable guidance in the simulation of the COSMOS 1408 event.

References

Anselmo, L., Pardini, C., 2017. An index for ranking active debris removal targets in leo. In: 7th European Conference on Space Debris. ESA Space Debris Office, Darmstadt-ESOC, pp. 18–21.

Bombardelli, C., Alessi, E., Rossi, A. et al., 2017. Environmental effect of space debris repositioning. Adv. Space Res., 60(1), 28–37. URL: https://www.sciencedirect.com/science/article/pii/S0273117717302491. doi: 10.1016/j.asr.2017.03.044.

Colombo, C., Letizia, F., Trisolini, M., et al., 2017. Life cycle assessment indicator for space debris.

Frey, S., Colombo, C., 2021. Transformation of satellite breakup distribution for probabilistic orbital collision hazard analysis. J. Guid., Control, Dynam., 44(1), 88–105. URL: doi: 10.2514/1.G004939. doi:10.2514/1.G004939. arXiv:https://doi.org/10.2514/1.G004939.

Grattagliano, P., Mignocchi, A., Montaruli, M.F. et al., 2025. Early stage characterization of on-orbit fragmentation events. Acta Astronaut., 236, 32–46. URL: https://www.sciencedirect.com/science/article/pii/S0094576525003418. doi: 10.1016/j.actaastro.2025.05.059.

Johnson, N., Krisko, P., Liou, J.-C. et al., 2001. Nasa's new breakup model of evolve 4.0. Adv. Space Res., 28(9), 1377–1384. URL: https://www.sciencedirect.com/science/article/pii/S0273117701004239. doi: 10.1016/S0273-1177(01)00423-9.

Kebschull, C., Scheidemann, P., Hesselbach, S. et al., 2017. Simulation of the space debris environment in leo using a simplified approach. Adv. Space Res., 59(1), 166–180. URL: https://www.sciencedirect.com/science/article/pii/S0273117716304380. doi: 10.1016/j.asr.2016.08.005.

Kelso, T., 2009. Analysis of the iridium 33-cosmos 2251 collision. In: Proceedings of the 19th AIAA/AAS Astrodynamics Specialist Conference, p. 135.

Klinner-Teo, T., Wacker, D.R., Djuren, R. et al., 2026. Dynamic scaling of fragment populations in orbital breakup modelling. Acta Astronaut., 246, 692–700. URL: https://www.sciencedirect.com/science/article/pii/S0094576526002894. doi: 10.1016/j.actaastro.2026.04.055.

LeoLabs, 2021. Analysis of the cosmos 1408 breakup. https://leolabs-space.medium.com/analysis-of-the-cosmos-1408-breakup-71b32de5641f.

Letizia, F., Colombo, C., Lewis, H. et al., 2017. Extending the ecob space debris index with fragmentation risk estimation.

Letizia, F., Colombo, C., Lewis, H.G. et al., 2016. Assessment of breakup severity on operational satellites. Adv. Space Res., 58(7), 1255–1274. URL: https://www.sciencedirect.com/science/article/pii/S0273117716302393. doi: 10.1016/j.asr.2016.05.036.

Morselli, A., Armellin, R., Di Lizia, P. et al., 2014. A high order method for orbital conjunctions analysis: sensitivity to initial uncertainties. Adv. Space Res., 53(3), 490–508. URL: https://www.sciencedirect.com/science/article/pii/S0273117713007412. doi: 10.1016/j.asr.2013.11.038.

Muciaccia, A., Facchini, L., Montaruli, M.F. et al., 2024. Radar observation and recontruction of cosmos 1408 fragmentation. J. Space Saf. Eng., 11 (1), 143–149. URL: https://www.sciencedirect.com/science/article/pii/S2468896723001131. doi: 10.1016/j.jsse.2023.11.006.

Muciaccia, A., Giudici, L., Letizia, F. et al., 2025. Evaluating the environmental impact of space missions. Acta Astronaut., 236, 239–250. URL: https://www.sciencedirect.com/science/article/pii/S0094576525003765. doi: 10.1016/j.actaastro.2025.06.024.

Olivieri, L., Giacomuzzo, C., Lopresti, S., et al., 2024. Simulation of in-space fragmentation events. Aerotecnica Missili & Spazio 103 (3), 225–232. https://doi.org/10.1007/s42496-023-00186-1.

Pardini, C., Anselmo, L., 2011. Physical properties and long-term evolution of the debris clouds produced by two catastrophic collisions in earth orbit. Adv. Space Res., 48(3), 557–569. URL: https://www.sciencedirect.com/science/article/pii/S0273117711002432. doi: 10.1016/j.asr.2011.04.006.

Pardini, C., Anselmo, L., 2016. Characterization of abandoned rocket body families for active removal. Acta Astronaut., 126, 243–257. URL: https://www.sciencedirect.com/science/article/pii/S0094576516301333. doi: 10.1016/j.actaastro.2016.04.035. Space Flight Safety.

Pardini, C., Anselmo, L., 2023. The short-term effects of the cosmos 1408 fragmentation on neighboring inhabited space stations and large constellations. Acta Astronaut., 210, 465–473. URL: https://www.sciencedirect.com/science/article/pii/S0094576523001078. doi: 10.1016/j.actaastro.2023.02.043.

Picone, J.M., Hedin, A.E., Drob, D.P. et al., 2002. Nrlmsise-00 empirical model of the atmosphere: Statistical comparisons and scientific issues. J. Geophys. Res.: Space Phys., 107(A12), SIA 15–1–SIA 15–16. URL: https://agupubs.onlinelibrary.wiley.com/doi/abs/10.1029/2002JA009430. doi: 10.1029/2002JA009430. arXiv:https://agupubs.onlinelibrary.wiley.com/doi/pdf/10.1029/2002JA009430.

Rossi, A., Alessi, E.M., Valsecchi, G.B., et al., 2017. A quantitative evaluation of the environmental impact of the mega constellations. In: 7th European Conference on Space Debris, p. 61.

Rossi, A., Petit, A., McKnight, D., 2020. Short-term space safety analysis of leo constellations and clusters. Acta Astronaut., 175, 476–483. URL: https://www.sciencedirect.com/science/article/pii/S0094576520303830. doi: 10.1016/j.actaastro.2020.06.016.

Rossi, A., Valsecchi, G., Alessi, E., 2015. The criticality of spacecraft index. Adv. Space Res., 56(3), 449–460. URL: https://www.sciencedirect.com/science/article/pii/S0273117715001556. doi: 10.1016/j.asr.2015.02.027. Advances in Asteroid and Space Debris Science and Technology - Part 1.

Rossi, A., Vellutini, E., Alessi, E. et al., 2022. Environmental index for fragmentation impact and environment evolution analysis. J. Space Safety Eng., 9(2), 269–273. URL: https://www.sciencedirect.com/science/article/pii/S2468896722000180. doi: 10.1016/j.jsse.2022.02.014.

Servadio, S., Simha, N., Gusmini, D. et al., 2024. Risk index for the optimal ranking of active debris removal targets. J. Spacecr. Rock., 61 (2), 407–420. URL: doi: 10.2514/1.A35752. doi:10.2514/1.A35752. arXiv:https://doi.org/10.2514/1.A35752.

Smith, T., Folcik, Z., Linares, R., 2024. Challenges in orbital debris modeling: a comparative analysis of nasa sbm and space fence data. In: Advanced Maui Optical and Space Surveillance (AMOS) Technologies Conference, p. 137.

Utzmann, J., Oswald, M., Stabroth, S., et al., 2012. Ranking and characterization of heavy debris for active removal. In: Proc. 63rd International Astronautical Congress.

Vallado, D., 2022. Fundamentals of Astrodynamics and Applications. Springer.